Nuclear Science and Techniques (2024) 35:166
https://doi.org/10.1007/s41365-024-01559-2

Properties of the phase diagram from the Nambu-Jona-Lasino model with a scalar-vector interaction

Yong-Hang Yang[1,2] · He Liu[1,2] · Peng-Cheng Chu[1,2]

Received: 28 April 2024 / Revised: 21 July 2024 / Accepted: 25 July 2024 / Published online: 18 September 2024
© The Author(s), under exclusive licence to China Science Publishing & Media Ltd. (Science Press), Shanghai Institute of Applied Physics, the Chinese Academy of Sciences, Chinese Nuclear Society 2024

Abstract
We investigated the properties of the phase diagram of high-order susceptibilities, speed of sound, and polytropic index based on an extended Nambu-Jona-Lasinio model with an eight-quark scalar-vector interaction. Non-monotonic behavior was observed in all these quantities around the phase transition boundary, which also revealed the properties of the critical point. Further, this study indicated that the chiral phase transition boundary and critical point could vary depending on the scalar-vector coupling constant G_{SV}. At finite densities and temperatures, the negative G_{SV} term exhibited attractive interactions, which enhanced the critical point temperature and reduced the chemical potential. The G_{SV} term also affected the properties of the high-order susceptibilities, speed of sound, and polytropic index near the critical point. The non-monotonic (peak or dip) structures of these quantities shifted to a low baryon chemical potential (and high temperature) with a negative G_{SV}. G_{SV} also changed the amplitude and range of the nonmonotonic regions. Therefore, the scalar-vector interaction was useful for locating the phase boundary and critical point in QCD phase diagram by comparing the experimental data. The study of the non-monotonic behavior of high-order susceptibilities, speed of sound, and polytropic index is of great interest, and further observations related to high-order susceptibilities, speed of sound, and polytropic index being found and applied to the search for critical points in heavy-ion collisions and the study of compact stars are eagerly awaited.

Keywords QCD phase diagram · High-order susceptibilities · Speed of sound · Polytropic index · NJL model

1 Introduction

The search for a first-order phase transition and critical point (CP) in the Quantum Chromodynamics (QCD) phase diagram is a fundamental goal of relativistic heavy-ion collision experiments [1–4]. Lattice QCD (LQCD) simulations have shown that the phase transition between the quark-gluon plasma (QGP) and hadronic matter is a smooth crossover at nearly zero baryon chemical potential ($\mu_{\mathrm{B}} \sim 0$) [5–7]. Based on investigations from various effective models, such as the Nambu–Jona-Lasinio (NJL) model and quark-meson (QM) model, as well as advanced functional methods including the Dyson-Schwinger equation (DSE) and functional renormalization group (FRG) [8–20], the transition can be of the first-order in the large μ_{B} region, resulting in a critical end point on the first-order phase transition line. However, different theoretical models and methods exhibit significant differences in the predicted CP location, even for the same model with different parameter sets [21]. To further explore the QCD phase diagram and search for a possible CP signal, experimental programs such as the Beam-Energy Scan (BES) are currently underway at the Relativistic Heavy-Ion Collider (RHIC). These involve varying the collision energy of heavy-ion collisions to cover a wide range of temperatures T and μ_{B} in the QCD phase diagram [22–24]. In the BES program, physical observations sensitive to CP and/or first-order phase transitions have been made, such as the

This work was supported by the National Natural Science Foundation of China (Nos. 12205158 and 11975132) and the Shandong Provincial Natural Science Foundation, China (Nos. ZR2021QA037, ZR2022JQ04 and ZR2019YQ01).

✉ He Liu
liuhe@qut.edu.cn

✉ Peng-Cheng Chu
kyois@126.com

1 Science School, Qingdao University of Technology, Qingdao 266520, China

2 The Research Center of Theoretical Physics, Qingdao University of Technology, Qingdao 266033, China

pion Hanbury-Brown Twiss (HBT) radii [25, 26], baryon directional flow [27, 28], net proton fluctuation [29, 30], light nuclear yield ratio [31–33], and interaction of charged hadrons [34]. Although nonmonotonic dependencies of these observations on collision energy have been observed, significant uncertainties remain in the nonmonotonic energy range.

Fluctuations in the conserved charges such as net charge, net baryon number, and net strangeness are predicted to depend on the nonequilibrium correlation length (ξ), which diverges at the singular critical point in the ideal system. However, they are typically limited by the finite size or the finite time of the system, and thus serve as possible signals of CP of the strongly interacting QCD matter created in relativistic heavy-ion collisions [35, 36]. Recent reports from first phase of the beam energy scan program (BES-I) of the RHIC [29, 30] demonstrated the non-monotonic variation of high-order moments of proton multiplicity (replacing the net baryon number) with collision energy in the range $7.7\,\mathrm{GeV} < \sqrt{s_{\mathrm{NN}}} < 27\,\mathrm{GeV}$. The measured higher-order moments refer to the skewness ($S = \langle(\delta N)^3\rangle/\sigma^3$) and kurtosis ($\kappa = \langle(\delta N)^4\rangle/\sigma^4 - 3$), where $\delta N = N - M$, M is the mean and σ is the quadratic variance. Furthermore, the cumulant ratio, $C_4/C_2 = \kappa\sigma^2$, of proton multiplicity distribution from $\sqrt{s_{\mathrm{NN}}} = 3.0\,\mathrm{GeV}$ Au + Au collisions was reported [24]. Compared with the Poisson baseline, a significant suppression in protons $C_4/C_2 = -0.85$ was observed in the most central $0\% - 5\%$ collisions at 3 GeV. This can be explained by fluctuations driven by baryon number conservation in a region of high baryon density, where hadronic interactions are dominant. These results imply that the QCD critical region, if created in heavy-ion collisions, can only exist at energies higher than 3 GeV. Light nuclei production has been suggested for exploring the existence and location of the QCD first-order phase-transition region with a corresponding critical point. In the 0–10% most central Au + Au collisions at $\sqrt{s_{\mathrm{NN}}} = 19.6\,\mathrm{GeV}$ and 27 GeV, $N_{\mathrm{t}} \times N_{\mathrm{p}}/N_{\mathrm{d}}^2$ shows enhancements relative to the coalescence baseline, with a combined significance of 4.1_{σ} [33]. Further studies on heavy-ion collisions are required to confirm whether these nonmonotonic dependencies are due to large fluctuations near the CP and to narrow the energy range at which CP may occur.

Hydrodynamics simulations provide another option for exploring QCD phase transitions. The spatiotemporal evolution of QCD matter can be successfully described using relativistic dissipative hydrodynamics [37–39]. The speed of sound is a crucial physical quantity in hydrodynamics, which carries important information for describing the evolution of strongly interacting matter and final observables in heavy-ion collision experiments. According to Ref. [40–42], the speed of sound as a function of the charged particle multiplicity $\langle \mathrm{d}N_{\mathrm{ch}}/\mathrm{d}\eta\rangle$ can be extracted from heavy-ion collision data. A recent study Ref. [43] estimated the value of c_{s} as well as its logarithmic derivative with respect to the baryon number density and attempted to build a connection with the cumulants of the net baryon number in matter created in heavy-ion collisions to aid in detecting the QCD CP. Furthermore, the behavior of c_s as a function of the baryon number density influences the equation of state (EOS) of neutron star matter. An EOS with a pronounced peak in the speed of sound was found to leave a clear and unique signature in the main frequency of the postmerger gravitational wave (GW) spectrum [44], which can sensitively probe the hadron-quark phase transition in the dense core. However, the polytropic index, defined as $\gamma \equiv \partial \ln P/\partial \ln \varepsilon$, is potentially important for determining the presence of quark matter in the core of massive neutron stars [45–48]. The approximate rule that $\gamma < 1.75$ [45] or $\gamma \leq 1.6$ and $c_{\mathrm{s}}^2 \leq 0.7$ [49] can be used as a good criterion for separating quark matter from hadronic matter in a massive neutron star core. A recent study [50] introduced a new conformality criterion quantity $d_{\mathrm{c}} \equiv \sqrt{\Delta^2 + (\Delta')^2}$, where $\Delta \equiv (\varepsilon - 3P)/(3\varepsilon)$ and $\Delta' \equiv \mathrm{d}\Delta/\mathrm{d}\ln\varepsilon$ are the normalized trace anomaly and its logarithmic rate of change with respect to the energy density, respectively, and compared d_{c} with the speed of sound, polytropic index, and normalized trace anomaly. The results indicate that the conformality criterion $d_{\mathrm{c}} < 0.2$ is considerably more restrictive than the criterion $\gamma < 1.75$ for quark matter in compact stars. Therefore, the speed of sound and polytropic index can serve as new probes for QCD CP or first-order phase transitions in future experimental exploration.

We utilized the significant findings of phase diagrams and critical points in the experimental and theoretical research mentioned above in recent years to explore the properties of QCD phase diagrams in the present work by calculating high-order moments, speed of sound, and polytropic index in an extended 3-flavor NJL model including an eight-quark scalar-vector interaction. Scalar-vector interactions are important for reproducing nuclear saturation properties when using the NJL-type model for nuclear matter [51]. When applied to the hadron-quark phase transition, the strength of the scalar-vector interactions can change the critical temperature T_{c}, thereby facilitating the study of the effect of CP in heavy-ion collisions [52, 53]. The remainder of this paper is organized as follows. In Sect. 2, we briefly review the calculation process of the extended 3-flavor NJL model, as well as the calculation formulas for the high-order moments, speed of sound, and polytropic index. The phase diagram of the high-order moments, speed of sound, and polytropic index, as well as the effects of the scalar-vector interaction on the phase diagram, are discussed in Sect. 3. Finally, the summary is presented in Sect. 4.

2 Theoretical model

The Lagrangian density of the extended three-flavor NJL model with an eight-quark scalar-vector interaction is given by [53]

$$\begin{aligned}\mathcal{L}_{\mathrm{NJL}}^{SU(3)} = & \bar{\psi}(i\gamma^{\mu}\partial_{\mu} - \hat{m})\psi + G_{\mathrm{S}} \sum_{a=0}^{8} \left[(\bar{\psi}\lambda^{a}\psi)^2 + (\bar{\psi}i\gamma_5\lambda^{a}\psi)^2\right] \\ & - K[\det\bar{\psi}(1+\gamma_5)\psi + \det\bar{\psi}(1-\gamma_5)\psi] \\ & + G_{\mathrm{SV}}\left\{\sum_{a=1}^{3}\left[(\bar{\psi}\lambda^{a}\psi)^2 + (\bar{\psi}i\gamma_5\lambda^{a}\psi)^2\right]\right\} \\ & \times \left\{\sum_{a=1}^{3}\left[(\bar{\psi}\gamma^{\mu}\lambda^{a}\psi)^2 + (\bar{\psi}\gamma_5\gamma^{\mu}\lambda^{a}\psi)^2\right]\right\},\end{aligned} \tag{1}$$

where $\psi = (u, d, s)^{\mathrm{T}}$ represents the three flavor quark fields and $\hat{m} = diag(m_{\mathrm{u}}, m_{\mathrm{d}}, m_{\mathrm{s}})$ is the corresponding current quark mass matrix. In the above formula, $\lambda^{a}(a = 1, \ldots, 8)$, where $\lambda^0 = \sqrt{2/3}$ are the Gell-Mann matrices; G_{S} and G_{SV} are the strengths of the scalar coupling and scalar-vector coupling, respectively; and the K term is the six-quark interaction (also known as the Kobayashi-Maskawa-t'Hooft interaction) that breaks the axial $U_{\mathrm{A}}(1)$ symmetry [54, 55]. This term gives rise to six-point interactions in the three flavors and is responsible for the flavor mixing effect.

In the mean-field approximation [56], quarks can be treated as quasiparticles whose constituent mass M_i is determined by the gap equation

$$\begin{aligned}M_{\mathrm{u}} = & m_{\mathrm{u}} - 2G_{\mathrm{S}}\phi_{\mathrm{u}} + 2K\phi_{\mathrm{d}}\phi_{\mathrm{s}} \\ & - 2G_{\mathrm{SV}}(\rho_{\mathrm{u}} + \rho_{\mathrm{d}})^2(\phi_{\mathrm{u}} + \phi_{\mathrm{d}}), \\ M_{\mathrm{d}} = & m_{\mathrm{d}} - 2G_{\mathrm{S}}\phi_{\mathrm{d}} + 2K\phi_{\mathrm{u}}\phi_{\mathrm{s}} \\ & - 2G_{\mathrm{SV}}(\rho_{\mathrm{u}} + \rho_{\mathrm{d}})^2(\phi_{\mathrm{u}} + \phi_{\mathrm{d}}), \\ M_{\mathrm{s}} = & m_{\mathrm{s}} - 2G_{\mathrm{S}}\phi_{\mathrm{s}} + 2K\phi_{\mathrm{u}}\phi_{\mathrm{d}},\end{aligned} \tag{2}$$

where $\phi_i = \langle\bar{i}i\rangle$ and ρ_i denote the quark condensate and net quark number densities, respectively. The thermodynamic properties of the three-flavor quark matter are determined by the partition function $\mathcal{Z} = Tr[\exp[-\beta(\hat{H} - \mu\hat{N})]]$. Here, $\beta = 1/T$ and μ are the reciprocals of the temperature and chemical potential, respectively, while $\hat{H}$ and $\hat{N}$ represent the Hamiltonian and the corresponding conserved charge number operators, respectively. The thermodynamic potential of the system can be calculated as

$$\begin{aligned}\Omega_{\mathrm{NJL}}^{SU(3)} = & G_{\mathrm{S}}(\phi_{\mathrm{u}}^2 + \phi_{\mathrm{d}}^2 + \phi_{\mathrm{s}}^2) + 3G_{\mathrm{SV}}(\phi_{\mathrm{u}} + \phi_{\mathrm{d}})^2(\rho_{\mathrm{u}} + \rho_{\mathrm{d}})^2 \\ & - 4K\phi_{\mathrm{u}}\phi_{\mathrm{d}}\phi_{\mathrm{s}} - 2N_{\mathrm{c}}\sum_{i=u,d,s}\int_0^{\Lambda}\frac{\mathrm{d}^3p}{(2\pi)^3}E_i \\ & - 2T\sum_{i=u,d,s}\int_0^{\Lambda}\frac{\mathrm{d}^3p}{(2\pi)^3}(z^{+}(E_i) + z^{-}(E_i)),\end{aligned} \tag{3}$$

where $N_{\mathrm{c}} = 3$ is the number of colors and

$$z^{\pm}(E_i) = N_{\mathrm{c}}\ln\left[1 + e^{-\beta(E_i \mp \tilde{\mu}_i)}\right], \tag{4}$$

with an effective chemical potential

$$\begin{aligned}\tilde{\mu}_{\mathrm{u}} &= \mu_{\mathrm{u}} + 2G_{\mathrm{SV}}(\rho_{\mathrm{u}} + \rho_{\mathrm{d}})(\phi_{\mathrm{u}} + \phi_{\mathrm{d}})^2, \\ \tilde{\mu}_{\mathrm{d}} &= \mu_{\mathrm{d}} + 2G_{\mathrm{SV}}(\rho_{\mathrm{u}} + \rho_{\mathrm{d}})(\phi_{\mathrm{u}} + \phi_{\mathrm{d}})^2, \\ \tilde{\mu}_{\mathrm{s}} &= \mu_{\mathrm{s}}.\end{aligned} \tag{5}$$

The energy E_i is expressed as $E_i = \sqrt{M_i^2 + p^2}$, where M_i is the mass of the constituent quarks. The quark condensate ϕ_i and net quark number density ρ_i can be derived by minimizing the thermodynamic potential as follows:

$$\begin{aligned}\phi_i = & 2N_{\mathrm{c}}\int\frac{\mathrm{d}^3p}{(2\pi)^3}\frac{M_i}{E_i}(f_i + \bar{f}_i - 1), \\ \rho_i = & 2N_{\mathrm{c}}\int\frac{\mathrm{d}^3p}{(2\pi)^3}(f_i - \bar{f}_i),\end{aligned} \tag{6}$$

where

$$\begin{aligned}f_i = & \frac{1}{1 + e^{\beta(E_i - \tilde{\mu}_i)}}, \\ \bar{f}_i = & \frac{1}{1 + e^{\beta(E_i + \tilde{\mu}_i)}}.\end{aligned} \tag{7}$$

In the present numerical calculation, we employ the following values for the parameters [57] as $m_{\mathrm{u}} = m_{\mathrm{d}} = 5.5\,\mathrm{MeV}$, $m_{\mathrm{s}} = 135.7\,\mathrm{MeV}$, $G_{\mathrm{S}}\Lambda^2 = 3.67$, $K\Lambda^5 = 9.29$, and the cutoff value in the momentum integral $\Lambda = 631.4\,\mathrm{MeV}$. For the coupling constant G_{SV}, Eqs. (2) and (5) show that its value can affect the effective masses of the quarks and their effective chemical potentials. However, the entire term, including G_{SV} does not affect the description of QCD vacuum properties at zero baryon density. Furthermore, treating the value of G_{SV} as a free parameter allows us to obtain the different properties of quark matter.

In the following section, we consider the fluctuation moments of conserved quantities, such as the net baryon number, from the above 3-flavor NJL model. The experimentally measured proton multiplicity (net baryon number) distributions are described by the moments or ratios of the cumulants. The relationships between the cumulants C_n and moments are defined as $C_1 = M$, $C_2 = \sigma^2$, $C_3 = S\sigma^3$, and $C_4 = \kappa\sigma^4$. Here, M and σ are the mean and quadratic variance, respectively, while the skewness S and kurtosis κ refer to higher-order moments. The ratios of the cumulants are often used to reduce the volume dependence, which can be read as $C_2/C_1 = \sigma^2/M$, $C_3/C_2 = S\sigma$, and $C_4/C_2 = \kappa\sigma^2$. Moreover, the ratios of cumulants in the theoretical calculations are related to the ratios of the baryon-number susceptibilities. The nth-order susceptibility of the net baryon number in the grand ensemble can be expressed as the derivative of the thermodynamic potential [58]

$$\chi_n^{\mathrm{B}} = \frac{\partial^n(-\Omega/T)}{\partial(\mu_{\mathrm{B}}/T)^n}. \tag{8}$$

The ratios of the baryon-number susceptibilities related to the skewness $S\sigma$ and kurtosis $\kappa\sigma^2$ measured experimentally in relativistic heavy-ion collisions can be calculated using [58]

$$S\sigma(B) = \frac{C_3^{\mathrm{B}}}{C_2^{\mathrm{B}}} = \frac{\chi_3^{\mathrm{B}}}{\chi_2^{\mathrm{B}}}, \quad \kappa\sigma^2(B) = \frac{C_4^{\mathrm{B}}}{C_2^{\mathrm{B}}} = \frac{\chi_4^{\mathrm{B}}}{\chi_2^{\mathrm{B}}}. \tag{9}$$

In heavy-ion collision experiments, the speed of sound c_{s} is a crucial thermodynamic observable, which provides important information for describing the evolution of the fireball. Recently, the authors in Ref. [43] attempted to build a connection between c_{s} and the cumulants of the baryon number distribution in matter created in heavy-ion collisions to aid in detecting QCD CP. The general definition of the speed of sound is $c_{\mathrm{s}}^2 = \partial P/\partial\varepsilon$, and its calculation requires specifying the thermodynamic variables that are kept constant. For the QGP created in relativistic heavy-ion collisions, it evolves with a constant entropy per baryon s/ρ_{B}, which justifies using the adiabatic speed of sound $c_{s/\rho_{\mathrm{B}}}$. In contrast, the isothermal speed of sound, c_{T}, is widely used in neutron star matter. However, the values of $c^2_{s/\rho_{\mathrm{B}}}$ and c_{T}^2 largely coincide near the critical point [59, 60], implying that the cumulants of the baryon number distribution in heavy-ion collisions can be used to estimate the isothermal squared speed of sound [43]. Therefore, in this study, we mainly discuss the phase diagram properties of the isothermal speed of sound. The pressure and entropy density in the NJL model can be derived using the thermodynamic relations in the grand canonical ensemble as follows:

$$P = -\Omega_{\mathrm{NJL}}, \quad s = -\frac{\partial\Omega_{\mathrm{NJL}}}{\partial T}, \tag{10}$$

and the energy density can be calculated as

$$\varepsilon = -P + Ts + \mu_{\mathrm{B}}\rho_{\mathrm{B}}. \tag{11}$$

Using the Jacobi method and thermodynamic relations, c_{T}^2 can be written in terms of T and μ_{B} as

$$c_{\mathrm{T}}^2 = \left(\frac{\partial P}{\partial\varepsilon}\right)_{\mathrm{T}} = \frac{\rho_{\mathrm{B}}}{T\left(\frac{\partial s}{\partial\mu_{\mathrm{B}}}\right)_{\mathrm{T}} + \mu_{\mathrm{B}}\left(\frac{\partial\rho_{\mathrm{B}}}{\partial\mu_{\mathrm{B}}}\right)_{\mathrm{T}}}. \tag{12}$$

Meanwhile, the polytropic index introduced in [45] $\gamma \equiv \partial\ln P/\partial\ln\varepsilon$ serves as a criterion for separating hadronic and quark matter [45, 47–49]. The isothermal polytropic index can be derived using the expression for the speed of sound:

$$\gamma_{\mathrm{T}} = \left(\frac{\partial P}{\partial\varepsilon}\right)_{\mathrm{T}} \Big/ \frac{P}{\varepsilon} = \frac{\varepsilon}{P}c_{\mathrm{T}}^2. \tag{13}$$

The above expression shows that the speed of sound is an important intermediate quantity for calculating the polytropic index. The differences between these two quantities may lead to a polytropic index that includes more intricate features near the phase boundary, which could potentially provide a new probe for exploring QCD CP.

3 Results and discussions

First, we discuss the higher-order susceptibilities of the net baryon number in the $\mu_{\mathrm{B}} - T$ plane based on the 3-flavor NJL model with different scalar-vector coupling constants G_{SV}. As shown in Fig. 1, we present the skewness $S\sigma(B)$ and kurtosis $\kappa\sigma^2(B)$ of the baryon number fluctuations as functions of temperature and baryon chemical potential. The red and blue regions represent positive and negative values, respectively, and the green regions represent the values of $S\sigma(B)$ and $\kappa\sigma^2(B)$ that are approximately zero. The black dashed-dotted and solid lines represent the chiral crossover and first-order phase transition, respectively, while the white dots connecting the chiral crossover and first-order phase transition represent the CPs. The chiral phase transition boundaries separate the red and blue regions for skewness, whereas the phase boundaries for kurtosis pass through the blue regions and divide the red regions with the CP located at the ends of the blue regions. In addition, the phase transition boundaries and CPs vary depending on the scalar-vector coupling constants G_{SV}. Although decreasing the value of G_{SV} effectively enhances the temperature of the CP, its baryon chemical potential decreases. The effects of G_{SV} can be understood using Eq. (2) and (5). According to Eq. (5), the negative G_{SV} resembles a vector interaction in the NJL model, which induces a repulsive interaction among the quarks. Meanwhile, compared with the scalar term G_{S} in the NJL model, a negative G_{SV} counteracts the repulsive interaction, as shown in Eq. (2), which reduces the constituent quark mass. For quark matter at a low baryon density (or chemical potential), the repulsive quark interaction with a negative G_{SV} is stronger than the attractive quark interaction [53, 57], resulting in

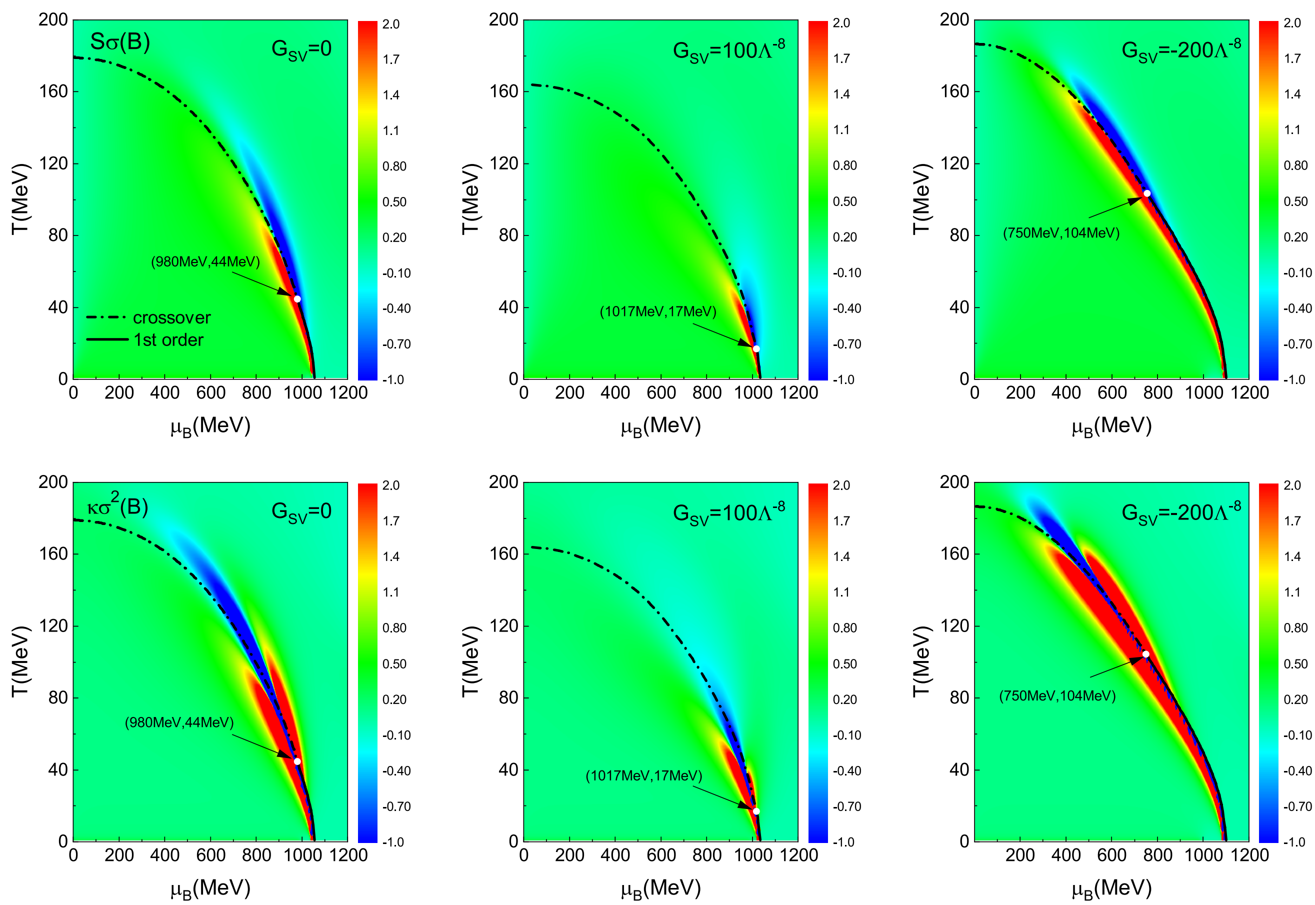

Fig. 1 (Color online) Skewness $S\sigma(B)$ and kurtosis $\kappa\sigma^2(B)$ of the baryon number fluctuations as functions of the temperature and baryon chemical potential in the NJL model with different scalar-vector coupling constants $G_{\rm SV}$. The black dash-dotted and solid lines represent the chiral crossover and first-order phase transition, respectively, while the white dots connecting the chiral crossover and first-order phase transition represent the CPs

a net repulsive effect of the negative $G_{\rm SV}$. For quark matter at intermediate densities, because the quadratic of $G_{\rm SV}$ term in Eq. (2) depends on the quark density, the effect of the $G_{\rm SV}$ term on constituent quark masses is significantly enhanced with increasing quark density, which generates an effectively attractive interaction among quarks. Consequently, when the coupling constant $G_{\rm SV} = -200\Lambda^{-8}$, the CP temperature increases to 104 MeV, while the chemical potential decreases to 750 MeV. For a positive $G_{\rm SV}$, the effects on the properties of quark matter are opposite to those of a negative $G_{\rm SV}$ leading to a lower temperature and higher baryon chemical potential CP. Therefore, the range of the CP location obtained by varying $G_{\rm SV}$ is sufficiently large to cover the region that can be probed during heavy-ion collisions. In quark matter at very high densities, where the chiral symmetry is largely restored and the quark condensates are close to zero, the effects of the $G_{\rm SV}$ term become less important. This differs from the usual vector interaction in the NJL model that becomes stronger at high densities.

In relativistic heavy-ion collision experiments, fluctuations in the net baryon number and net charge number were measured at the chemical freeze-out lines. However, the location of chemical freeze-out could not be accurately determined at the RHIC-BES energies. Several criteria exist for chemical freeze-out, such as fixed energy per particle at approximately 1 GeV, fixed total density of baryons and antibaryons, fixed entropy density over T^3, and the percolation model. Recently, the hypothetical freeze-out lines derived by fitting the experimental data have been expressed as $T = a - b\mu_{\rm B}^2 - c\mu_{\rm B}^4$ [2, 61]. However, the exact correspondence between the experimental parameters and location on the phase diagram remains unclear. Therefore, for simplicity and better elucidation of the properties of the phase diagram near the critical point, the hypothetical freeze-out lines shown in Fig. 2 were obtained by rescaling $\mu_{\rm B}$ of the phase boundaries with factors of 0.90, 0.95, 0.98, 1.02, and 1.05, which can also be found in Refs. [16, 20, 62]. Figure 3 shows the skewness $S\sigma(B)$ and kurtosis $\kappa\sigma^2(B)$ of the net baryon number fluctuations as functions of the baryon

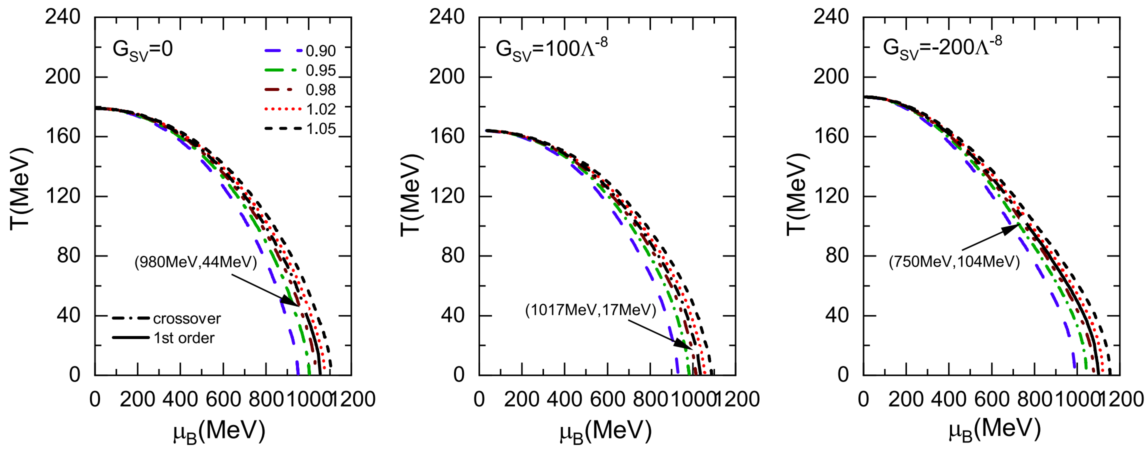

Fig. 2 (Color online) Hypothetical chemical freeze-out lines with different scalar-vector coupling constants G_{SV} by rescaling μ_{B} of the chiral phase transition boundary with factors of 0.90, 0.95, 0.98, 1.02, and 1.05

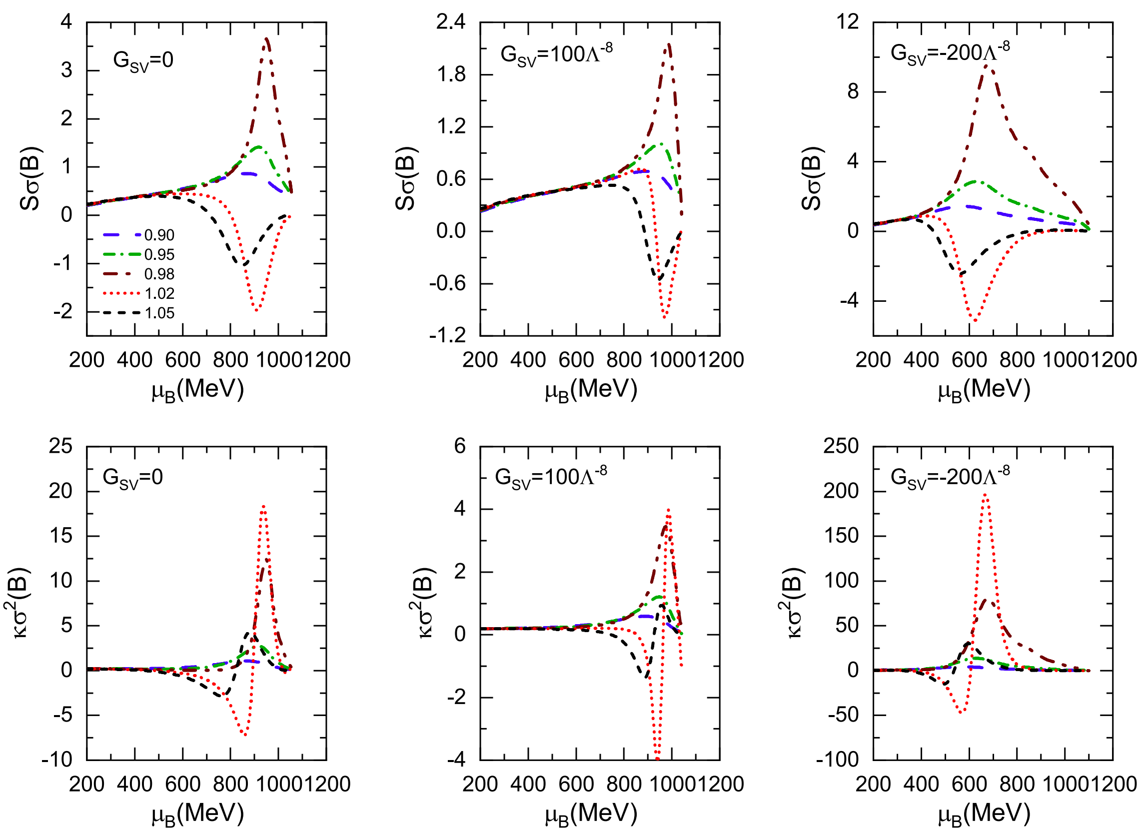

Fig. 3 (Color online) Skewness $S\sigma(B)$ and kurtosis $\kappa\sigma^2(B)$ of the net baryon number fluctuations as functions of the baryon chemical potential along the hypothetical chemical freeze-out lines with different scalar-vector coupling constants G_{SV}

chemical potential along the hypothetical chemical freeze-out lines with different scalar-vector coupling constants G_{SV}. Along the hypothetical chemical freeze-out lines, non-monotonic dependencies in both $S\sigma(B)$ and $\kappa\sigma^2(B)$ occur, and peak or dip structures appear around the critical points. In contrast, $\kappa\sigma^2(B)$ features both a positive peak and negative dip, whereas $S\sigma(B)$ has either a single peak or dip, whose nature (peak or dip) depends on whether the hypothetical freeze-out lines are below the chiral phase transition boundaries. The amplitude of the peak or dip structures increases significantly as the hypothetical chemical freeze-out lines approach the CPs, for example, along the hypothetical lines with factors of 0.98 and 1.02. The nonmonotonic behavior of $\kappa\sigma^2(B)$ is qualitatively consistent with the experimental results, while the experimental results for $S\sigma(B)$ seem to be positive above $\sqrt{s_{NN}} = 7.7$ GeV from both STAR and PHENIX measurements [27]. Further experiments on collisions of different heavy ions at different energies are required, so that the freeze-out lines are close to or even above the phase transition boundaries. In addition, the peak and dip structures of the net-baryon susceptibilities shift to the low-baryon chemical potential (and high-temperature) side with a negative scalar-vector coupling constant G_{SV}, which is consistent with our previous discussions and expectations. Furthermore, the amplitudes of variation for both $S\sigma(B)$ and $\kappa\sigma^2(B)$ values significantly increase as G_{SV} decreases, which may be because G_{SV} is a quartic term in the thermodynamic potential. Thus, fluctuations in the density and quark condensation near the CP are greatly amplified.

The speed of sound, which is a fundamental property of a substance, provides important information for describing the evolution of strongly interacting matter and the final observables in heavy-ion collision experiments. It can be obtained from heavy-ion collision data through the charged particle multiplicity $\langle dN_{ch}/d\eta \rangle$ [40–42]. Furthermore, the net baryon fluctuations in heavy-ion collisions can be used to estimate the isothermal speed of sound and its logarithmic derivative [43]. The numerical results from effective models [59, 60, 67] suggest that the speed of sound at the CP is the global minimum of the full phase diagram and is also considered a sensitive probe of the hadron-quark phase transition in the compact star core. Figure 4 presents the contour maps of the squared speed of sound c_T^2 in the $\mu_B - T$ plane based on the NJL model with different scalar-vector coupling constants G_{SV}. The values of c_T^2 in the chiral breaking regions corresponding to the blue regions are mostly less than 0.2. For the different scalar-vector coupling constants G_{SV}, changes in the range of chiral breaking (blue) regions and the location of the critical points are evident. After passing through the chiral phase transition boundary, c_T^2 rapidly increases with the restoration of chiral symmetry. In Fig. 4, a dip structure appears on the low-temperature side of the chiral phase transition boundary, and a minimum of c_T^2 appears around the critical point. For the different scalar-vector coupling constants, the value of c_T^2 is less than 1 in the entire $\mu_B - T$ plane, satisfying the constraint of causality. However, in the NJL model, c_T^2 does not approach the value $c_s^2 = 1/3$ of conformal matter limit at the high temperatures and baryon chemical potentials, because of the cutoff parameter set for the momentum integral in the NJL model. For the Polyakov-looped Nambu-Jona-Lasinio (PNJL) model, because momentum integration is finite and does not require an ultraviolet cutoff [11, 12], the squared speed of sound at high temperatures and baryon chemical potentials approaches 1/3 [60]. To further explore the properties of the speed of sound near the critical points, we present the results of the squared speed of sound c_T^2 along the hypothetical chemical freeze-out lines with different scalar-vector coupling constants G_{SV} in Fig. 5. For the hypothetical freeze-out lines over the chiral phase transition boundaries, the c_T^2 curves rapidly increase after softening near the CPs. However, the speed of sound along the hypothetical freeze-out lines below the chiral phase transition boundary varies considerably: c_T^2 rapidly decreases near the CPs, especially as it approaches the local minimum along the curve by a factor of 0.98, followed by a spinodal behavior that eventually continues to decrease. Additionally, the spinodal regions are influenced by G_{SV}. As G_{SV} decreases, the span of the spinodal regions

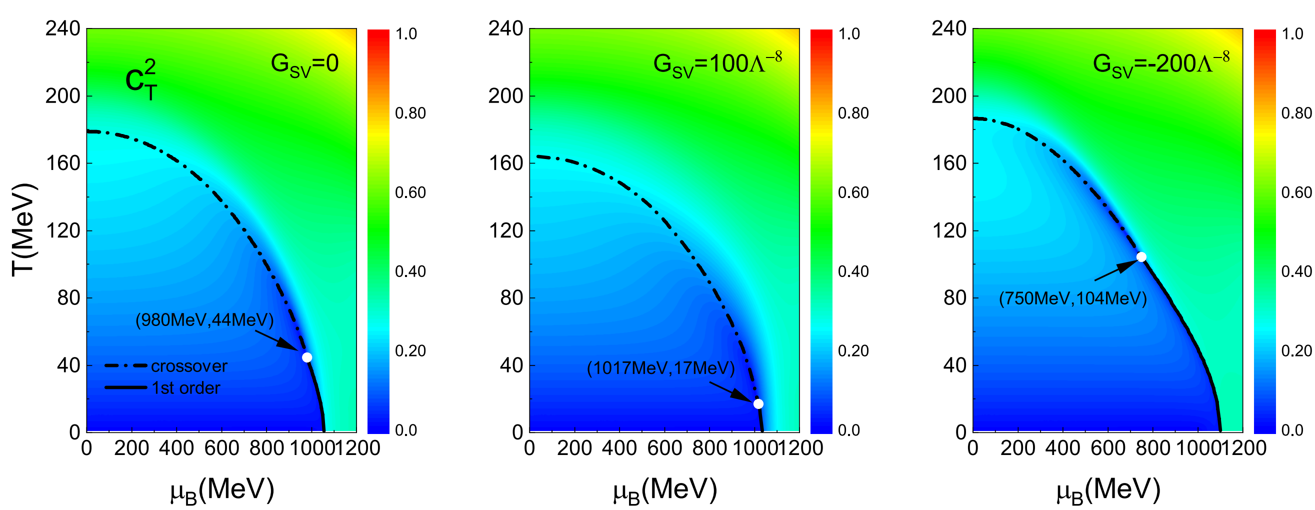

Fig. 4 (Color online) Contour maps of the squared speed of sound c_T^2 in the $\mu_B - T$ plane based on the NJL model with different scalar-vector coupling constants G_{SV}. The black dash-dotted and solid lines indicate the chiral crossover and first-order phase transition, respectively, while the white dots connecting the chiral crossover and first-order phase transition represent the critical points (CPs)

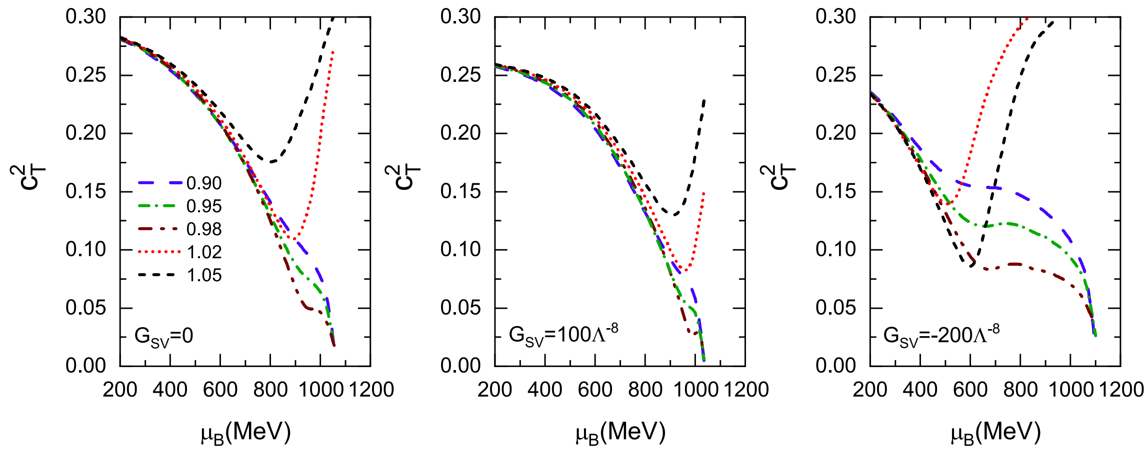

Fig. 5 (Color online) Squared speed of sound c_T^2 as a function of baryon chemical potential along the hypothetical chemical freeze-out lines with different scalar-vector coupling constants G_{SV}

expands accordingly; conversely, it decreases or approaches zero with increasing G_{SV}. This is also observed in Fig. 1, where the positive G_{SV} reduces the amplitude of the fluctuations around the critical points.

Subsequently, we investigated the contour maps of the polytropic index γ_T in the $\mu_B - T$ plane with different G_{SV} values, as shown in Fig. 6. The values of γ_T are almost less than 1.5 in the chiral breaking regions with different G_{SV}. On either side of the phase boundary, particularly around the first-order phase transition, non-monotonic behavior, including dip (blue region) and peak (red region) structures in γ_T are clearly observed. Following an isotherm that passes through a first-order phase transition, the polytropic index rapidly decreases to a minimum value, increases rapidly to the maximum with chiral restoration, and subsequently decreases again, eventually stabilizing at high temperatures and baryon chemical potentials. This can be explained by Eq. (13), where the polytropic index is equal to the squared speed of sound divided by P/ε. Around the first-order phase transition, the squared speed of sound (the derivative of P with respect to ε) and P/ε are not synchronized; therefore, a local minimum and maximum of the polytropic index appear at different chemical potentials. A more detailed explanation is provided in Ref. [60]. In Fig. 6, the amplitudes and spans of the dip and peak structures are influenced by the coupling constants G_{SV}. The amplitude and span of the peak structures (red regions) are effectively enhanced by decreasing the value of G_{SV}; however, those of the dip structures (blue regions) decrease. Similar to the speed of sound, we investigate the properties of γ_T along the hypothetical chemical

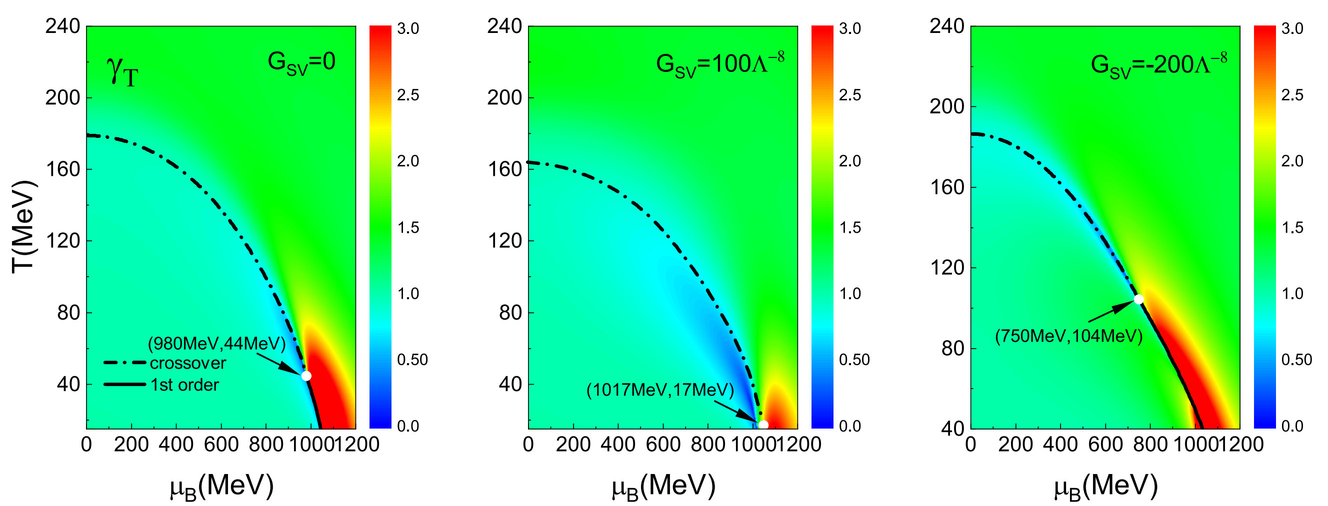

Fig. 6 (Color online) Contour maps of the polytropic index γ_T in the $\mu_B - T$ plane based on the NJL model with different scalar-vector coupling constants G_{SV}. The black dash-dotted and solid represent the chiral crossover and first-order phase transition, respectively, and the white dots connecting the chiral crossover and first-order phase transition represent the critical points (CPs)

freeze-out lines in Fig. 7. All curves of γ_T first decrease and attain a minimum near the CP, and closer critical points correspond to smaller minimum values, such as the hypothetical freeze-out lines with 0.98 or 1.02. Consistent with the results for $S\sigma(B)$ and $\kappa\sigma^2(B)$, the mininum value of γ_{T} shifts to a low baryon chemical potential with a negative G_{SV}. Further, a negative G_{SV} leads to a larger minimum value of γ_{T} because the negative G_{SV}, which serves as a repulsive interaction at a low chemical potential, stiffens the equation of stateand increases the speed of sound and polytropic index. Compared to c_{T}^2 as shown in Fig. 5, the polytropic index exhibits a more pronounced dip structure near the CP, which could provide a more sensitive probe for the QCD CP in future experiments.

4 Summary and outlook

In conclusion, we investigated the properties of the phase diagrams of higher-order susceptibilities, speed of sound, and polytropic index based on an extended NJL model with an eight-quark scalar-vector interaction. We found that all the aforementioned quantities exhibited non-monotonic behavior around the phase transition boundaries, which also revealed the location of the critical point. Specifically, the baryon susceptibility $\kappa\sigma^2(B)$ featured both a positive peak and negative dip, whereas $S\sigma(B)$ had either a single peak or dip, whose nature depended on whether the hypothetical freeze-out lines were below the phase-transition boundaries. Meanwhile, for c_{T}^2, a dip structure appeared on the low-temperature side of the phase transition boundary, and a minimum appeared around the critical point. Along the hypothetical freeze-out lines below the phase transition boundary, the speed of sound rapidly decreased near the CP, followed by spinodal behavior, whereas the polytropic index γ_{T} exhibited a more pronounced dip as it approached the CP. Compared to the speed of sound, the polytropic index could provide a more sensitive probe for QCD CP in future experiments. In this study, we explored the effect of the eight-quark scalar-vector interaction on the phase diagram. The chiral phase transition boundary and critical point varied depending on the scalar-vector coupling constants G_{SV}. At finite densities and temperatures, the negative G_{SV} term exhibited attractive interactions, which enhanced the critical point temperature and reduced the chemical potential. The G_{SV} term also affected the high-order susceptibilities, speed of sound, and polytropic index. The nonmonotonic (peak or dip) structures of these quantities shifted to a low baryon chemical potential (and high temperature) with a negative G_{SV}. G_{SV} also changed the amplitude and range of the non-monotonic regions. Therefore, the scalar-vector interaction is useful for locating the phase boundary and critical point in the QCD phase diagram by comparing the experimental data. Although significant uncertainty remains regarding the properties of the QCD phase diagram and the precise location of the critical point, the study of the non-monotonic behavior of these observables is of great interest. A more accurate BES-II measurement in the near future will provide further information regarding the QCD phase diagram. Moreover, in the study of massive neutron stars, the approximate rule $\gamma < 1.75$ [45] or $\gamma \leq 1.6$ and $c_s^2 \leq 0.7$ may be used as a good criterion for separating quark matter from hadronic matter in a massive neutron star core [49]. Recently, a new conformality criterion $d_c < 0.2$, defined as comprising γ and c_s, was introduced and compared with the speed of sound, polytropic index, and normalized trace anomaly [50]. The results indicate that the conformality criterion $d_c < 0.2$ is considerably more restrictive than the criterion $\gamma < 1.75$ for quark matter in compact stars [50]. In recent years, machine learning (ML)and high-energy nuclear physics have begun

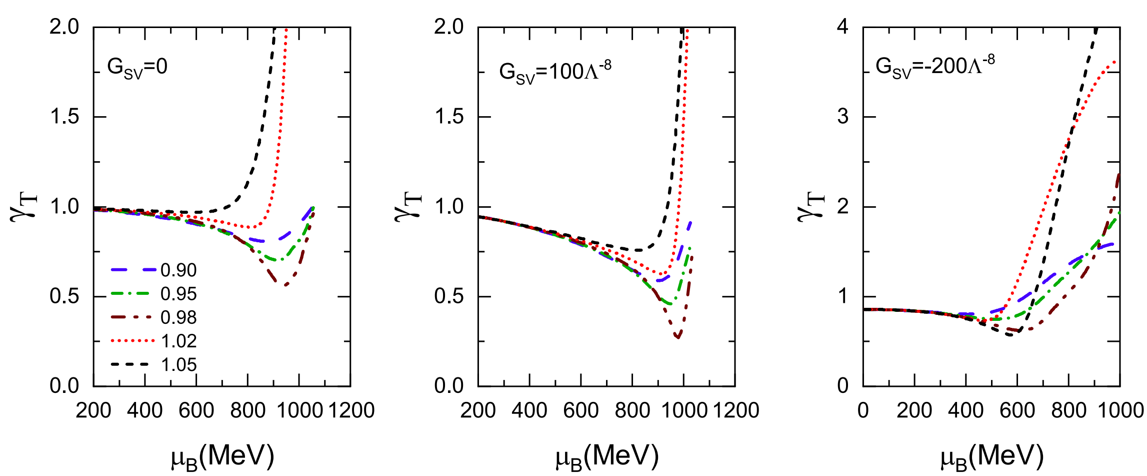

Fig. 7 (Color online) Polytropic index γ_{T} as a function of the baryon chemical potential along the hypothetical chemical freeze-out lines for different scalar-vector coupling constants G_{SV}

to merge, yielding interesting results [67]. ML methods have also been applied to phase transition studies, enabling finer characterization of the QCD phase diagram and deeper understanding of quark matter properties [68]. Therefore, it is worth looking forward to new methods and observations related to high-order susceptibilities, speed of sound, and polytropic index and their application to the search for critical points in heavy-ion collisions and the study of compact stars.

Author Contributions All authors contributed to the study conception and design. Material preparation, data collection and analysis were performed by Yong-Hang Yang, He Liu and Peng-Cheng Chu. The first draft of the manuscript was written by Yong-Hang Yang and all authors commented on previous versions of the manuscript. All authors read and approved the final manuscript.

Data Availability The data that support the findings of this study are openly available in Science Data Bank at https://cstr.cn/31253.11.sciencedb.j00186.00225 and https://doi.org/10.57760/sciencedb.j00186.00225.

Declarations

Conflict of interest The authors declare that they have no Conflict of interest.

References

1. P. Braun-Munzinger, V. Koch, T. Schäfer et al., Properties of hot and dense matter from relativistic heavy ion collisions. Phys. Rep. **621**, 76 (2016). https://doi.org/10.1016/j.physrep.2015.12.003
2. X. Luo, N. Xu, Search for the QCD critical point with fluctuations of conserved quantities in relativistic heavy-ion collisions at RHIC: an overview. Nucl. Sci. Tech. **28**, 112 (2017). https://doi.org/10.1007/s41365-017-0257-0
3. Y. Zhang, D.W. Zhang, X.F. Luo, Experimental study of the QCD phase diagram in relativistic heavy-ion collisions. Nucl. Tech. (in Chinese) **46**, 040001 (2023). https://doi.org/10.11889/j.0253-3219.2023.hjs.46.040001
4. A. Bzdak, S. Esumi, V. Koch et al., Mapping the phases of quantum chromodynamics with beam energy scan. Phys. Rep. **853**, 1–87 (2020). https://doi.org/10.1016/j.physrep.2020.01.005
5. C. Bernard, T. Burch, E.B. Gregory et al., QCD thermodynamics with three flavors of improved staggered quarks. Phys. Rev. D **71**, 034504 (2005). https://doi.org/10.1103/PhysRevD.71.034504
6. Y. Aoki, G. Endrődi, Z. Fodor et al., The order of the quantum chromodynamics transition predicted by the standard model of particle physics. Nature **443**, 675 (2006). https://doi.org/10.1038/nature05120
7. A. Bazavov, T. Bhattacharya, M. Cheng et al., Chiral and deconfinement aspects of the QCD transition. Phys. Rev. D **85**, 054503 (2012). https://doi.org/10.1103/PhysRevD.85.054503
8. T.M. Schwarz, S.P. Klevansky, G. Papp, Phase diagram and bulk thermodynamical quantities in the Nambu-Jona-Lasinio model at finite temperature and density. Phys. Rev. C **60**, 055205 (1999). https://doi.org/10.1103/PhysRevC.60.055205
9. P. Zhuang, M. Huang, Z. Yang, Density effect on hadronization of a quark plasma. Phys. Rev. C **62**, 054901 (2000). https://doi.org/10.1103/PhysRevC.62.054901
10. W.J. Fu, Z. Zhang, Y.X. Liu, 2+1 flavor Polyakov-Nambu-Jona-Lasinio model at finite temperature and nonzero chemical potential. Phys. Rev. D **77**, 014006 (2008). https://doi.org/10.1103/PhysRevD.77.014006
11. K. Fukushima, Phase diagrams in the three-flavor Nambu-Jona-Lasinio model with the Polyakov loop. Phys. Rev. D **77**, 114028 (2008). https://doi.org/10.1103/PhysRevD.77.114028
12. K. Fukushima, Erratum: Phase diagrams in the three-flavor Nambu–Jona-Lasinio model with the Polyakov loop [Phys. Rev. D 77, 114028 (2008)]. Phys. Rev. D **78**, 039902 (2008). https://doi.org/10.1103/PhysRevD.78.039902
13. S.X. Qin, L. Chang, H. Chen et al., Phase diagram and critical end point for strongly interacting quarks. Phys. Rev. Lett. **106**, 172301 (2011). https://doi.org/10.1103/PhysRevLett.106.172301
14. X.Y. Xin, S.X. Qin, Y.X. Liu et al., Quark number fluctuations at finite temperature and finite chemical potential via the Dyson-Schwinger equation approach. Phys. Rev. D **90**, 076006 (2014). https://doi.org/10.1103/PhysRevD.90.076006
15. F. Gao, Y.X. Liu, QCD phase transitions using the QCD Dyson-Schwinger equation. Nucl. Tech. (in Chinese) **46**, 040015 (2023). https://doi.org/10.11889/j.0253-3219.2023.hjs.46.040015
16. J.W. Chen, J. Deng, H. Kohyama et al., Robust characteristics of non-Gaussian fluctuations from the NJL model. Phys. Rev. D **93**, 034037 (2016). https://doi.org/10.1103/PhysRevD.93.034037
17. H. Liu, J. Xu, L.W. Chen et al., Isospin properties of quark matter from a 3-flavor NJL model. Phys. Rev. D **94**, 065032 (2016). https://doi.org/10.1103/PhysRevD.94.065032
18. W.J. Fu, J.M. Pawlowski, F. Rennecke, QCD phase structure at finite temperature and density. Phys. Rev. D **101**, 054032 (2020). https://doi.org/10.1103/PhysRevD.101.054032
19. S. Yin, Y.Y. Tan, W.J. Fu, Critical phenomena and functional renormalization group. Nucl. Tech. (in Chinese) **46**, 040002 (2023). https://doi.org/10.11889/j.0253-3219.2023.hjs.46.040002
20. H. Liu, J. Xu, Isospin effect on baryon and charge fluctuations from the pNJL model. Universe **7**, 6 (2021). https://doi.org/10.3390/universe7010006
21. V. Vovchenko, J. Steinheimer, O. Philipsen et al., Cluster expansion model for QCD baryon number fluctuations: No phase transition at $\mu_B/\pi < T$. Phys. Rev. D **97**, 114030 (2018). https://doi.org/10.1103/PhysRevD.97.114030
22. M.M. Aggarwal et al., (STAR Collaboration), Higher moments of net proton multiplicity distributions at RHIC. Phys. Rev. Lett. **105**, 022302 (2010). https://doi.org/10.1103/PhysRevLett.105.022302
23. L. Adamczyk et al., (STAR Collaboration), beam energy dependence of moments of the net-charge multiplicity distributions in Au + Au collisions at RHIC. Phys. Rev. Lett. **112**, 032302 (2014). https://doi.org/10.1103/PhysRevLett.113.092301
24. M. Abdallah et al., (STAR Collaboration), measurements of proton high-order cumulants in 3 GeV Au + Au collisions and implications for the QCD critical point. Phys. Rev. Lett. **128**, 202303 (2022). https://doi.org/10.1103/PhysRevLett.128.202303
25. L. Adamczyk et al., (STAR Collaboration), Beam-energy-dependent two-pion interferometry and the freeze-out eccentricity of pions measured in heavy ion collisions at the STAR detector. Phys. Rev. C **92**, 014904 (2015). https://doi.org/10.1103/PhysRevC.92.014904
26. J. Adam et al., (STAR Collaboration), Flow and interferometry results from Au + Au collisions at 4.5 GeV. Phys. Rev. C **103**, 034908 (2021). https://doi.org/10.1103/PhysRevC.103.034908
27. L. Adamczyk et al., (STAR Collaboration), Beam-energy dependence of the directed flow of protons, antiprotons, and pions in Au + Au collisions. Phys. Rev. Lett. **112**, 162301 (2014). https://doi.org/10.1103/PhysRevLett.112.162301
28. L. Adamczyk et al., (STAR Collaboration), Beam-Energy Dependence of Directed Flow of Λ, $\bar{\Lambda}$, $K^{\pm}$, K_s^0, and ϕ in Collisions. Phys.

Rev. Lett. **120**, 062301 (2018). https://doi.org/10.1103/PhysRevLett.120.062301

29. J. Adam et al., (STAR Collaboration), Observation $D_s^{\pm}/D^0$ of Enhancement in Au + Au Collisions at =200 GeV. Phys. Rev. Lett. **126**, 092301 (2021). https://doi.org/10.1103/PhysRevLett.127.092301
30. M. Abdallah et al., (STAR Collaboration), Cumulants and correlation functions of net-proton, proton, and antiproton multiplicity distributions in Au +Au collisions at energies available at the BNL Relativistic Heavy Ion Collider. Phys. Rev. C **104**, 024902 (2021). https://doi.org/10.1103/PhysRevC.104.024902
31. K.J. Sun, L.W. Chen, C.M. Ko et al., Light nuclei production as a probe of the QCD phase diagram. Phys. Lett. B **781**, 499 (2018). https://doi.org/10.1016/j.physletb.2018.04.035
32. K.J. Sun, L.W. Chen, C.M. Ko et al., Light nuclei production and QCD phase transition in heavy-ion collisions. Nucl. Tech. (in Chinese) **46**, 040012 (2023). https://doi.org/10.11889/j.0253-3219.2023.hjs.46.040012
33. M.I. Abdulhamid et al., (STAR Collaboration), Beam energy dependence of triton production and yield ratio ($N_t \times N_p/N_d^2$) in Au + Au collisions at RHIC. Phys. Rev. Lett. **130**, 202301 (2023). https://doi.org/10.1103/PhysRevLett.130.202301
34. M.I. Abdulhamid et al., (STAR Collaboration), Energy dependence of intermittency for charged hadrons in Au+ Au collisions at RHIC. Phys. Lett. B **845**, 138165 (2023). https://doi.org/10.1016/j.physletb.2023.138165
35. M. Asakawa, U. Heinz, B. Müller, Fluctuation probes of quark deconfinement. Phys. Rev. Lett. **85**, 2072 (2000). https://doi.org/10.1103/PhysRevLett.85.2072
36. S. Jeon, V. Koch, in *Quark-Gluon Plasma 3*, edit by R.C. Hwa, X.N. Wang (World Scientific, Singapore, 2004), p. 430. https://doi.org/10.1142/5029
37. H.C. Song, S.A. Bass, U. Heinz et al., 200*A* GeV Au + Au collisions serve a nearly perfect quark-gluon liquid. Phys. Rev. Lett. **106**, 192301 (2011). https://doi.org/10.1103/PhysRevLett.106.192301
38. H.C. Song, S.A. Bass, U. Heinz, Viscous QCD matter in a hybrid hydrodynamic + Boltzmann approach. Phys. Rev. C **83**, 024912 (2011). https://doi.org/10.1103/PhysRevC.83.024912
39. P. Deb, G.P. Kadam, H. Mishra, Estimating transport coefficients in hot and dense quark matter. Phys. Rev. D **94**, 094002 (2016). https://doi.org/10.1103/PhysRevD.94.094002
40. R. Campanini, G. Ferri, Experimental equation of state in pp and pp collisions and phase transition to quark gluon plasma. Phys. Lett. B **703**, 237 (2011). https://doi.org/10.1016/j.physletb.2011.08.009
41. F.G. Gardim, G. Giacalone, M. Luzum et al., Revealing QCD thermodynamics in ultrarelativistic nuclear collisions. Nat. Phys. **16**, 615 (2020). https://doi.org/10.1038/s41567-020-0846-4
42. D. Sahu, S. Tripathy, R. Sahoo et al., Multiplicity dependence of shear viscosity, isothermal compressibility and speed of sound in pp collisions at 7 TeV. Eur. Phys. J. A **56**, 187 (2020). https://doi.org/10.1140/epja/s10050-020-00197-7
43. A. Sorensen, D. Oliinychenko, V. Koch et al., Speed of sound and baryon cumulants in heavy-ion collisions. Phys. Rev. Lett. **127**, 042303 (2021). https://doi.org/10.1103/PhysRevLett.127.042303
44. Y.J. Huang, L. Baiotti, T. Kojo et al., Merger and postmerger of binary neutron stars with a quark-hadron crossover equation of state. Phys. Rev. Lett. **129**, 181101 (2022). https://doi.org/10.1103/PhysRevLett.129.181101
45. E. Annala, T. Gorda, A. Kurkela et al., Evidence for quark-matter cores in massive neutron stars. Nat. Phys. **16**, 907 (2020). https://doi.org/10.1038/s41567-020-0914-9
46. H. Liu, J. Xu, P.C. Chu, Symmetry energy effects on the properties of hybrid stars. Phy. Rev. D **105**, 043015 (2022). https://doi.org/10.1103/PhysRevD.105.043015
47. H. Liu, X.M. Zhang, P.C. Chu, Properties of quark-matter cores in massive hybrid stars. Phys. Rev. D **107**, 094032 (2023). https://doi.org/10.1103/PhysRevD.107.094032
48. H. Liu, Y.H. Yang, Y. Han et al., Properties of quark matter and hybrid stars from a quasiparticle model. Phys. Rev. D **108**, 034004 (2023). https://doi.org/10.1103/PhysRevD.108.034004
49. M.Z. Han, Y.J. Huang, S.P. Tang et al., Plausible presence of quark matter in neutron stars with masses above $0.97M_{\rm TOV}$. Sci. Bull. **68**, 913 (2023). https://doi.org/10.1016/j.scib.2023.04.007
50. E. Annala, T. Gorda, J. Hirvonen et al., Strongly interacting matter exhibits deconfined behavior in massive neutron stars. Nat. Commun. **14**, 8451 (2023). https://doi.org/10.1038/s41467-023-44051-y
51. V. Koch, T.S. Biro, J. Kunz et al., A chirally invariant fermionic field theory for nuclear matter. Phys. Lett. B **185**, 1–5 (1987). https://doi.org/10.1016/0370-2693(87)91517-6
52. T.G. Lee, Y. Tsue, J. da Providencia et al., Quark-hadron phase-transition in an extended njl model with scalar-vector interaction. Prog. Theor. Exp. Phys. **2013**, 013D02 (2013). https://doi.org/10.1093/ptep/pts055
53. K.J. Sun, C.M. Ko, S. Cao et al., QCD critical point from the Nambu-Jona-Lasino model with a scalar-vector interaction. Phys. Rev. D **103**, 014006 (2021). https://doi.org/10.1103/PhysRevD.103.014006
54. G. t'Hooft, Computation of the quantum effects due to a four-dimensional pseudo-particle. Phys. Rev. D **14**, 3432 (1976). https://doi.org/10.1103/PhysRevD.14.3432
55. G. t'Hooft, Erratum: Computation of the quantum effects due to a four-dimensional pseudoparticle. Phys. Rev. D **18**, 2199 (1978). https://doi.org/10.1103/PhysRevD.18.2199.3
56. U. Vogl, W. Weise, The Nambu and Jona-Lasinio model: Its implications for Hadrons and Nuclei. Prog. Part. Nucl. Phys. **27**, 195 (1991). https://doi.org/10.1016/0146-6410(91)90005-9
57. M. Buballa, NJL-model analysis of dense quark matter. Phys. Rept. **407**, 205 (2005). https://doi.org/10.1016/j.physrep.2004.11.004
58. M. Asakawa, M. Kitazawa, Fluctuations of conserved charges in relativistic heavy ion collisions: An introduction. Prog. Part. Nucl. Phys. **90**, 299 (2016). https://doi.org/10.1016/j.ppnp.2016.04.002
59. W.B. He, G.Y. Shao, X.Y. Gao et al., Speed of sound in QCD matter. Phys. Rev. D **105**, 094024 (2022). https://doi.org/10.1103/PhysRevD.105.094024
60. H. Liu, Y.H. Yang, C. Yuan et al., Speed of sound and polytropic index in the Polyakov-loop Nambu-Jona-Lasinio model. Phys. Rev. D **109**, 074037 (2024). https://doi.org/10.1103/PhysRevD.109.074037
61. V.V. Begun, V. Vovchenko, M.I. Gorenstein, Updates to the p + p and A + A chemical freeze-out lines from the new experimental data. J. Phys. Conf. Ser. **779**, 012080 (2017). https://doi.org/10.1088/1742-6596/779/1/012080
62. J.W. Chen, J. Deng, H. Kohyama et al., Universal relations between non-Gaussian fluctuations in heavy-ion collisions. Phys. Rev. D **95**, 014038 (2017). https://doi.org/10.1103/PhysRevD.95.014038
63. W.B. He, G.Y. Shao, C.L. Xie, Speed of sound and liquid-gas phase transition in nuclear matter. Phys. Rev. C **107**, 014903 (2023). https://doi.org/10.1103/PhysRevC.107.014903
64. S.K. Ghosh, T.K. Mukherjee, M.G. Mustafa et al., Susceptibilities and speed of sound from the Polyakov-Nambu-Jona-Lasinio model. Phys. Rev. D **73**, 114007 (2006). https://doi.org/10.1103/PhysRevD.73.114007
65. R. Marty, E. Bratkovskaya, W. Cassing et al., Transport coefficients from the Nambu-Jona-Lasinio model for $SU(3)_f$. Phys. Rev. C **88**, 045204 (2013). https://doi.org/10.1103/PhysRevC.88.045204

66. K. Saha, S. Ghosh, S. Upadhaya et al., Transport coefficients in a finite volume Polyakov-Nambu-Jona-Lasinio model. Phys. Rev. D **97**, 116020 (2018). https://doi.org/10.1103/PhysRevD.97.116020
67. W.B. He, Y.G. Ma, L.G. Pang et al., High-energy nuclear physics meets machine learning. Nucl. Sci. Tech. **34**, 88 (2023). https://doi.org/10.1007/s41365-023-01233-z
68. Y.G. Ma, L.G. Pang, R. Wang et al., Phase transition study meets machine learning. Chin. Phys. Lett. **40**, 122101 (2023). https://doi.org/10.1088/0256-307X/40/12/122101

Springer Nature or its licensor (e.g. a society or other partner) holds exclusive rights to this article under a publishing agreement with the author(s) or other rightsholder(s); author self-archiving of the accepted manuscript version of this article is solely governed by the terms of such publishing agreement and applicable law.